Sensors and Actuators B 186 (2013) 734–740

Contents lists available at SciVerse ScienceDirect

Sensors and Actuators B: Chemical

journal homepage: www.elsevier.com/locate/snb

Flower-like WO_3 architectures synthesized via a microwave-assisted method and their gas sensing properties

Zhenyu Wang[a], Peng Sun[a], Tianlin Yang[a], Yuan Gao[a,*], Xiaowei Li[a], Geyu Lu[a,*], Yu Du[b]

[a] State Key Laboratory on Integrated Optoelectronics, College of Electronic Science and Engineering, Jilin University, 2699 Qianjin Street, Changchun 130012, People's Republic of China
[b] Department of Applied Physics, Shenzhen University, Shenzhen 518060, People's Republic of China

ARTICLE INFO

Article history:
Received 12 January 2013
Received in revised form 3 June 2013
Accepted 4 June 2013
Available online 14 June 2013

Keywords:
Flower-like
WO_3 architecture
NO_2 sensor
Microwave-assisted solvothermal

ABSTRACT

The flower-like WO_3 structures were successfully synthesized by a simple calcination of $W_{18}O_{49}$ nanowires obtained by a microwave-assisted solvothermal method. The as-prepared products were characterized by field emission scanning electron microscopy, X-ray powder diffraction, transmission electron microscopy, and nitrogen adsorption and desorption measurements. The results indicated that the building blocks of the flower-like structure were intercrossing single crystalline WO_3 nanorods with diameter of about 30–40 nm and length of about 300–400 nm. The gas sensing properties of as-prepared products to NO_2 and acetone were investigated. It was found that the sensor based on WO_3 nanostructures exhibited excellent selectivity and high sensitivity toward NO_2 at optimum temperature of 90 °C, giving a response of about 42 to 40 ppb NO_2. Significantly, operating at 300 °C, the sensor's response and recovery time to 100 ppm acetone was only 1 s and 6 s, respectively.

1. Introduction

In recent years, complex micro/nanostructures, especially three-dimensional (3D) hierarchical architectures that are assembled using 1D and 2D nanoscale building blocks including nanowires, nanobelts, nanoplatelets, nanotubes, etc., caused a lot of attention. Compared to solid structures, functional materials with hierarchical structure have some unique physical and chemical properties. So they will provide more opportunities for exploring novel properties and superior device performances, such as catalysis [1], adsorption [2], separation [3], self-cleaning [4], and so on. It is a precondition to assemble functional nanoscale building blocks into appropriate superstructures for electronic and optoelectronic applications of nanocrystals. Motivated by this, a lot of researches have been carried out for the synthesis of complex inorganic materials and investigating how architectures, sizes, morphologies, and patterns influence their collective optical, magnetic, and electronic properties. To prepare the hierarchical architectures, various routes have been employed successfully to assemble building blocks into 3D ordered superstructures [5–8]. However, these methods are either time-consuming or involve some additives, which possibly increase pollution or limit the potential applications. Consequently, it is strongly desirable to develop a simple, effective, and economical approach for the synthesis of 3D hierarchical nanostructures. Microwave-assisted hydrothermal/solvothermal method is one of the most promising methods due to its good characters such as energy-conserving, rapid, efficient, environment friendly. A variety of semiconductor nanomaterials with hierarchical structures have been successfully prepared using this route in the past few years, such as ZnO [9,10], Fe_2O_3/Fe_3O_4 [11,12], CuO [13,14], TiO_2 [15–17], and SnO_2 [18].

The metal oxide, as an important kind of functional materials, has tunable properties and important technological applications. Among them, tungsten oxide (WO_3), a N-type semiconductor with band-gap of 2.5 eV, has some unique and interesting properties which enable its application in many aspects, such as gas sensors [19], photocatalysts [20], electro/gas/photo chromic devices [21], field-emission devices [22], and solar-energy devices [23]. Much effort has been made to synthesize tungsten oxide with various nanostructures. To obtain those desired structures, a lot of efficient methods were involved, including template directed synthesis [24], solution-based approach [25], and chemical vapor deposition [26] and hydrothermal reactions [27]. Significantly, Yan et al. have reported WO_3 hydrate nanowire netted-spheres synthesized in the glycol solution using a facile solvothermal approach with F127 as surfactant [28]. Yella et al. reported tungsten oxide nanobrushes synthesized using a solvothermal approach in the presence of citric acid and hexadecylamine as surfactants [29]. According to these reports, surfactant plays an important role in the synthesis of WO_3 hierarchical architectures. So far, it is still a challenge to prepare WO_3 hie-structures without surfactant.

* Corresponding authors. Tel.: +86 431 85167808; fax: +86 431 85167808.
E-mail addresses: gaoyuan@jlu.edu.cn (Y. Gao), lugy@jlu.edu.cn (G. Lu).

0925-4005/$ – see front matter © 2013 Published by Elsevier B.V.
http://dx.doi.org/10.1016/j.snb.2013.06.015

Herein, we report the preparation of flower-like WO_3 hierarchical architectures by a simple surfactant-free microwave-assisted solvothermal process followed by calcination. To demonstrate a potential application of the material, the gas-sensing properties were investigated.

2. Experimental

WCl_6 (99%, Aladdin Chemical Reagent Company, Shanghai) and absolute ethanol (Beijing Chemical Reagent Company) were used as received without further purification. In a typical process, 0.2 g WCl_6 was added into 40 mL absolute ethanol. After stirring vigorously for 30 min, the homogeneous solution was transferred into a Teflon-liner and then put into a microwave digestion system (Ethos One, Milestone Inc., Italy), the reaction was conducted at 200 °C for 2 h. After cooling to room temperature by the inherent air-cooling system, the products were washed with deionized water and absolute ethanol by centrifugation for several times. After that, the as-prepared products were collected and dried at 80 °C for 10 h. In order to obtain the final flower-like WO_3, the precipitate was calcined at 500 °C for 2 h. X-ray power diffraction (XRD) analysis was conducted on a Rigaku D/max-2500 X-ray diffractometer with Cu-Kα1 radiation (λ = 0.15406 nm) and the scanning speed was 12° min^{-1}. Field emission scanning electron microscopy (FESEM) images were recorded on a JEOL JSM-7500F microscope operating at 15 kV. Transmission electron microscopy (TEM), selected-area electron diffraction (SAED), and high-resolution transmission electron microscopy (HRTEM) images were obtained on a JEOL JEM-200EX microscope with accelerating voltage of 200 kV and a JEOL JEM-3010 microscope operated at 200 kV, respectively. Thermogravimetric (TG) analysis and differential scanning calorimetric (DSC) measurements were carried out using a NETZSCH STA 449F3 simultaneous thermogravimetric analyzer under air atmosphere in the temperature range from 30 to 800 °C with a heating rate of 10 °C min^{-1}. The specific surface areas and the pore size distribution of the sample were characterized with Brunauer–Emmett–Teller (BET) method (Gemini VII, Micromeritics Co. Ltd.).

A sensor device was fabricated as follows: proper amount of the as-prepared WO_3 powder was mixed with deionized water to obtain a paste, and then coated on an Al_2O_3 ceramic tube (4 mm in length, 1.2 mm in external diameter, and 0.8 mm in internal diameter, attached with a pair of gold electrodes). After drying under a mercury lamp for 10 min, the tube was then sintered at 500 °C for 2 h. To keep the sensor working at elevated temperature, a Ni–Cr alloy coil was inserted into the ceramic tube as a heater. The gas-sensing properties of the sensor were measured with a static gas-sensing characterization system, as diagrammed in Fig. 1: the sensor was put into a closed glass chamber and a given amount of the tested gas was injected into the chamber for the measurement of the sensitive performance. The relative humidity in the measurement atmosphere is between 30% and 40%. The response of the sensor was defined as R_g/R_a and R_a/R_g for oxidizing gas and reducing gas, respectively, where R_a and R_g stand for the resistances of sensor in air and in the target gas.

3. Results and discussion

Fig. 2 shows the X-ray diffraction (XRD) patterns of the precursors prepared by microwave-assisted solvothermal process and the products obtained by calcining the precursors. As can be seen, before calcinations, the diffraction peaks could be indexed to the standard $W_{18}O_{49}$ with the monoclinic structure and matched well with the reported data (space group: P2/m, lattice constant a = 18.28 Å, b = 3.775 Å, c = 13.98 Å, beta = 115.2°, JCPDS: 5-392).

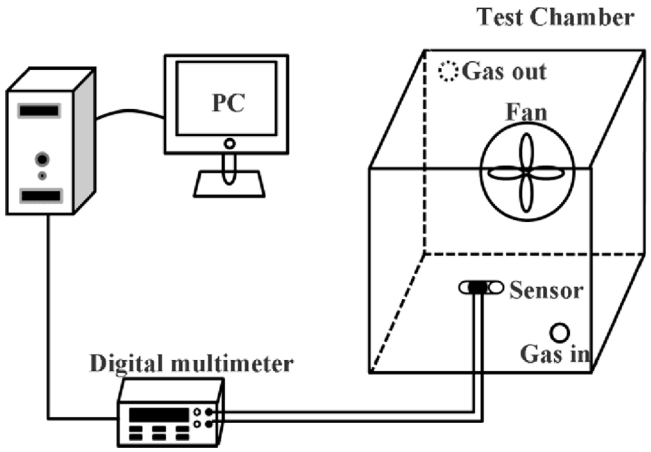

Fig. 1. Schematic illustration of sensor testing system.

After calcining at 500 °C for 2 h, the $W_{18}O_{49}$ precursors were thoroughly converted into pure monoclinic WO_3 according to JCPDS card no. 89-4476, with space group P21/n and lattice parameters of a = 7.3271 Å, b = 7.5644 Å, c = 7.7274 Å, beta = 90.488°. No other diffraction peaks were observed, indicating that no impurity existed and the $W_{18}O_{49}$ completely transformed into the WO_3.

The morphology, structure, and size of the samples were characterized with FESEM, TEM, and HRTEM. Fig. 3a corresponds to a SEM image of the $W_{18}O_{49}$ precursors. As can be seen, the precursors were nanowires with lengths about 1 μm and diameters about tens of nanometers. Fig. 3b is a typical SEM image of the as-synthesized WO_3 sample, from which a number of flower-like particles with diameters about 300–400 nm were clearly observed and the building blocks of the flower-like WO_3 architectures were a lot of intercrossing nanorods with diameters about 30–40 nm. Although a few of nanorods can be seen in sight, but most of the resultant showed a flower-like morphology, indicating a high yield of these flower-like architectures. It also can be observed that the sample was unconsolidated, what is a good character for gas sensing properties. The typical TEM image in Fig. 3c shows that the size and shape of WO_3 were corresponding well to those of the FESEM observations. Fig. 3d and e was the corresponding SAED pattern and the HRTEM image taken from a random nanorod on the flower-like WO_3 particles, respectively. Both of them confirmed

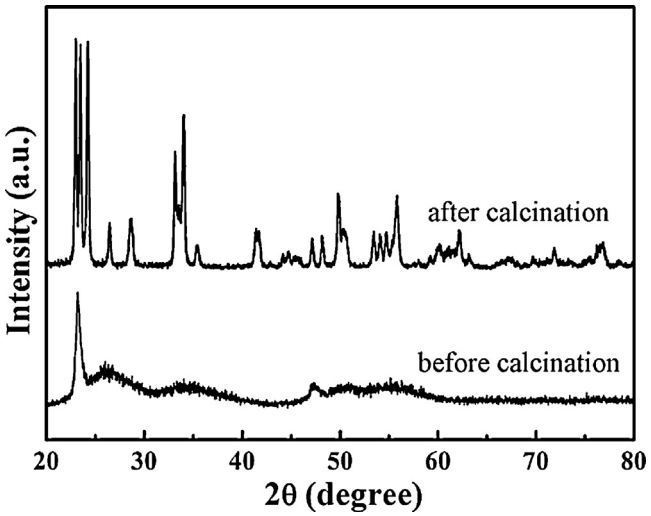

Fig. 2. X-ray diffraction patterns of the as-prepared samples before and after sintering.

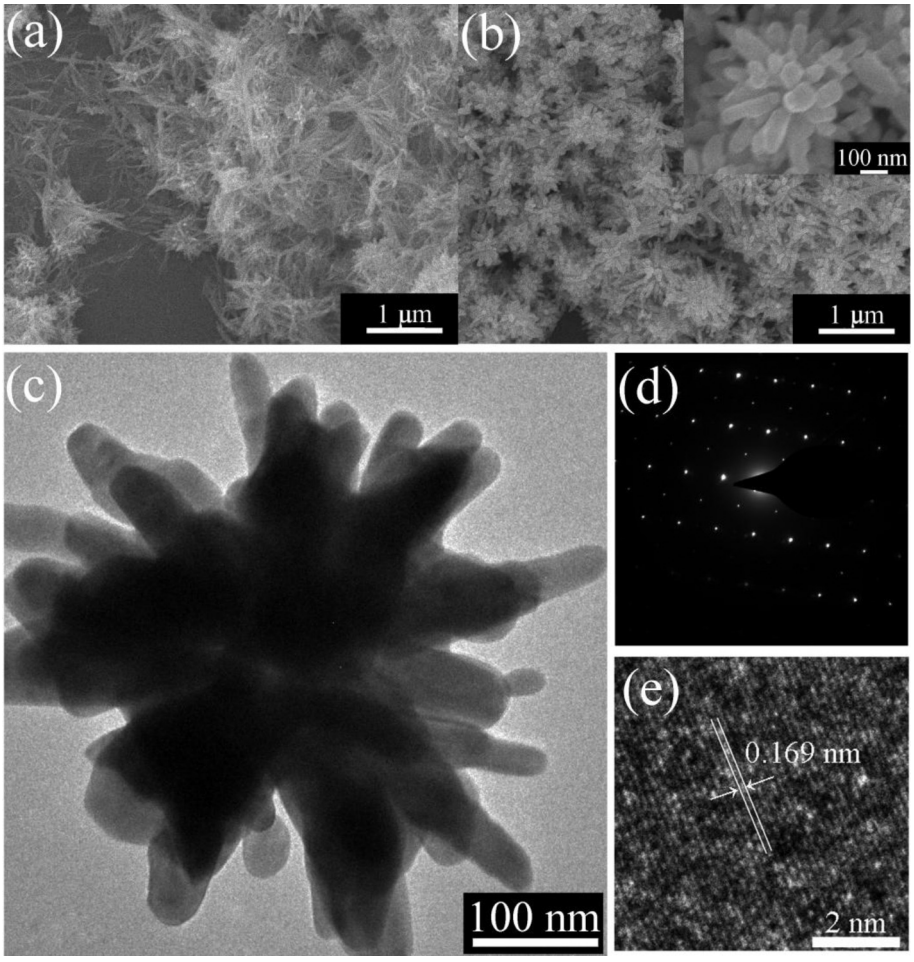

Fig. 3. Morphological characterization of as-synthesized samples: (a) FESEM image of $W_{18}O_{49}$, (b) FESEM images of WO_3 architectures, (c) TEM image of a flower-like particle, (d) HRTEM, and (e) SAED image of a randomly chosen nanorod on the flower-like architectures.

that the nanorods building up the flower-like architecture were single-crystalline structures.

From the SEM images we can see that after calcination the $W_{18}O_{49}$ nanowires became flower-like hierarchical structures which were composed of nanorods. The procedure can be described as follow: when annealing in air, on the first stage, the $W_{18}O_{49}$ precursors would be oxidized by reacting with oxygen and turn into WO_3. This stage can be described as the following equation:

$$2W_{18}O_{49} + 5O_2 \rightarrow 36WO_3 \quad (1)$$

Secondly, the obtained WO_3 would re-crystallize and begin to grow. At this stage, to lessen the free energy, those crystal grains will readjust to reduce grain boundaries in the material, consequently, the intercrossing nanowires became thicker and shorter, and those with a same intersection finally grew into a WO_3 flower-like architecture.

The N_2 adsorption–desorption isotherms and the corresponding BJH pore size distribution plot (inset) of the as-obtained WO_3 nanostructures are shown in Fig. 4. According to the IUPAC classification, flower-like WO_3 architectures show a type IV isotherm with a type H3 hysteresis loop. These are typical characteristics of mesoporous materials. The BET surface area and the pore volume of the WO_3 nanoparticles are 13.6 m^2/g and 0.09 cm^3/g, respectively. The inset reveals the corresponding pore size distribution derived by the Barret–Joyner–Halenda (BJH) method. From the curves, we can see that this sample has two peaks at the pore-size distribution plot about 11 nm and 61 nm, respectively, displays porous structures with a wide range of pore size distributions from 4 nm to 154 nm.

Thermogravimetric (TG) and differential scanning calorimetric (DSC) curves of the obtained precursors are displayed in Fig. 5. On the TG curve, the first weight loss, of 6.5% between 30 and 200 °C (endothermic DSC peak at 120 °C), corresponded to the removal of

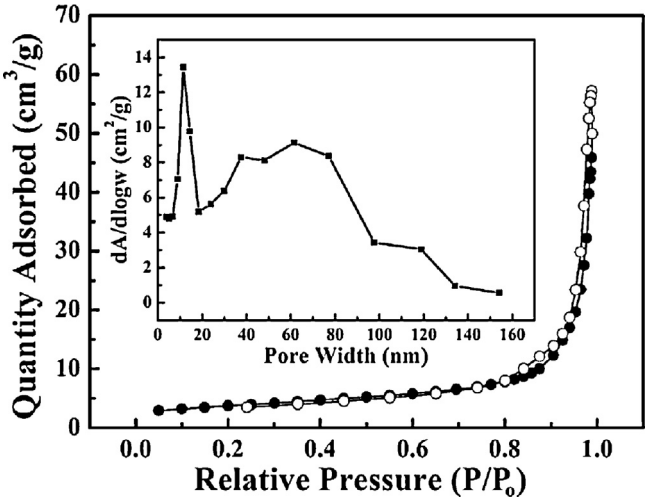

Fig. 4. Nitrogen adsorption–desorption isotherm and corresponding pore-size distribution of WO_3 powders.

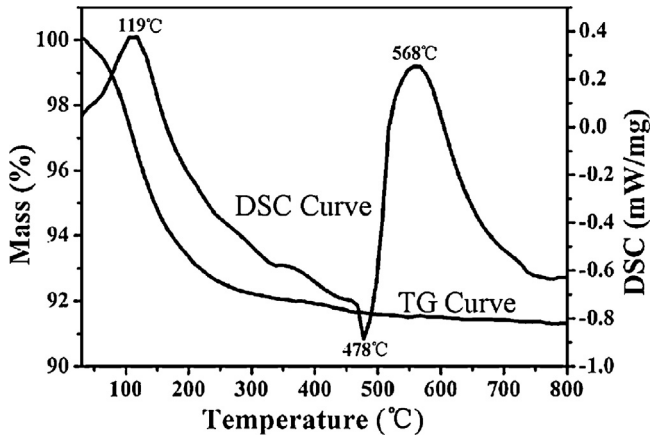

Fig. 5. TG and DSC curves of the as-synthesized $W_{18}O_{49}$ precursor.

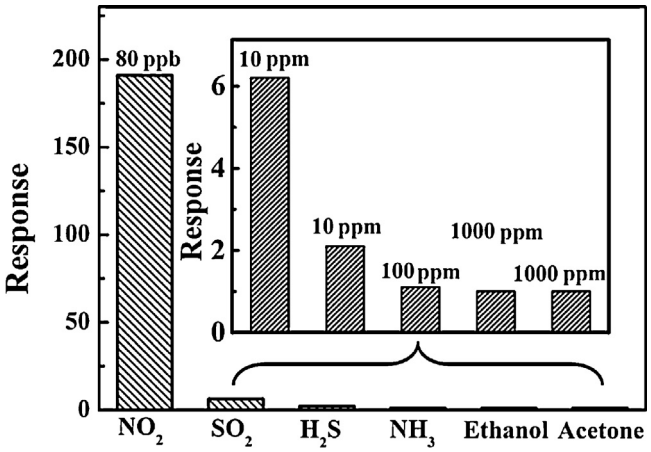

Fig. 7. Cross-responses to various gases for the sensor using the as-prepared WO_3 at 90 °C.

the water and those organics such as ethanol weakly adsorbed to the surface of $W_{18}O_{49}$. It can be seen that TG curve's slope became smaller between 200 and 500 °C, and the low weight loss (2%) in this range can be assigned to the weight gain during the $W_{18}O_{49}$ oxidation and the simultaneous weight loss caused by the organics removal. Over 500 °C the weight did not change significantly, which indicated that $W_{18}O_{49}$ had evolved to WO_3 and those organics had been removed thoroughly. After the thoroughly oxidation, the crystal continued to grow and the crystallinity improved, which was an exothermic process (corresponding to the 500–800 °C part of the DSC curve).

The sensing properties of the sensor based on the as-prepared WO_3 sample were investigated. In order to determine the optimum operating temperature, the responses of the sensor to 80 ppb NO_2 were measured at different temperatures, from 50 to 125 °C, as shown in Fig. 6. The response increased with a raise of operating temperature and reached the maximum value of 190.8 at 90 °C, followed by a decrease with further increase of operating temperature. Therefore, to further examine the characteristics of the sensor, the optimal operating temperature of 90 °C was chosen for NO_2 detecting. When the temperature increased from 50 to 90 °C, the increase of the response could be roughly explained as the increase of the surface reaction rate ($NO_{2(g)} + e^- \rightarrow NO_{2(ads)}^-$), but when the temperature further increased, the response might be limited by the low diffusion depth and began to decrease. At the optimum temperature (90 °C), the optimum balance between the reaction and diffusion depth has been established for the NO_2 molecules [30]. The characteristic of low temperature working makes the sensor significantly energy saving, which is corresponding to the pursuit of gas sensor design in recent years.

It is well-known that selectivity is one of the important parameter for the gas sensors. To test the selectivity of the sensor based on the as-prepared WO_3, the responses of the sensor to various testing gases at the operating temperature of 90 °C were tested, including two kinds of oxidation gases (NO_2, SO_2) and four kinds of reducing gases (H_2S, NH_3, acetone, and ethanol). In Fig. 7, the results indicate that the sensor using flower-like WO_3 particles exhibited much lower responses to H_2S and SO_2, than that of the response to NO_2, although the concentrations of them were much higher. And the sensor showed scarcely any response to 100 ppm NH_3 or 1000 ppm acetone and ethanol, which might can be attributed to the low operating temperature of the sensor. The highest response of the sensor was about 190.8 to 80 ppb NO_2, while the responses to other gases were no greater than 6.2. Therefore, it was concluded that the sensor using as-synthesized WO_3 nanoparticles showed selectivity toward NO_2 against other examined gases.

The relationship between response and NO_2 concentrations for the sensor at operating temperature is depicted in Fig. 8. The inset of Fig. 8 shows the sensor's gas response to lower concentration of NO_2 clearly. As can be seen, the response increased with the increase of NO_2 concentration from 5 to 80 ppb. It is worthy to notice that even when the sensor based on the as-prepared flower-like WO_3 exposed to only 5 ppb NO_2, the response can also

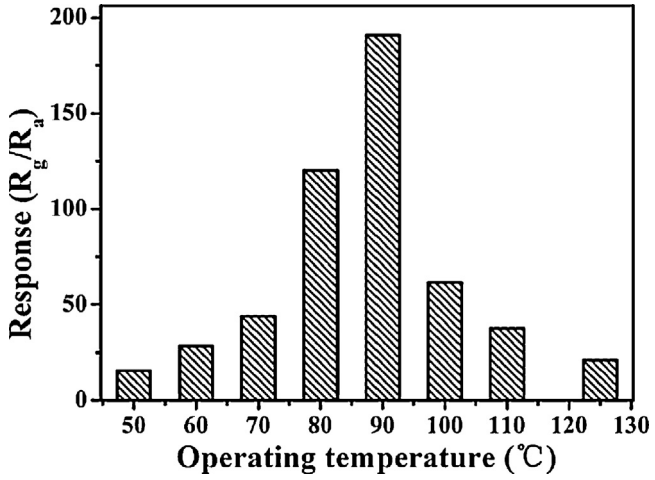

Fig. 6. Response of the sensor to 80 ppb NO_2 as a function of operating temperature.

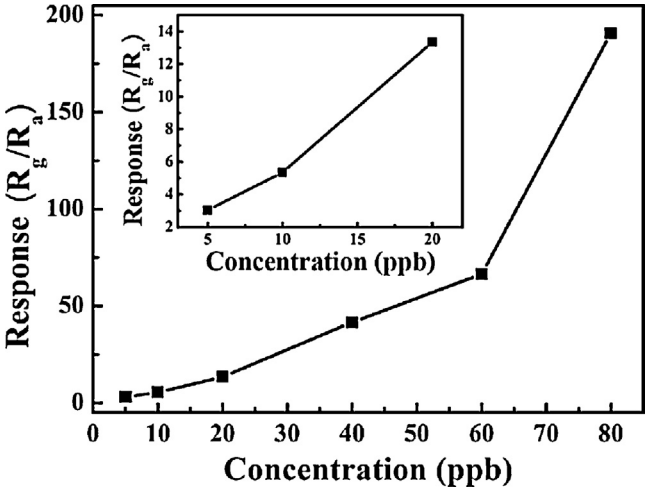

Fig. 8. Response of the sensor versus the NO_2 concentration at 90 °C.

Table 1
Gas responses to NO_2 in the present study and those reported in the literatures [19,31–34].

Material	Preparation	NO_2 concentration (ppb)	Operating temperature (°C)	R_g/R_a	References
WO_3	Hydrothermal	40	125	24	[31]
WO_3	Wet process	50	200	3	[32]
WO_3	Acidification	50	200	13	[19]
Re-WO_3	Wet process	50	200	15	[33]
MnO_2-WO_3	Sputtering	10	200	2	[34]
WO_3	Microwave assisted solvothermal	40	90	42	Present study
WO_3	Microwave assisted solvothermal	5	90	3	Present study

be measured. A comparison between the sensing performances of the sensor fabricated in our work and literature reports was summarized in Table 1. From comparison, it can be seen that the sensor using flower-like WO_3 nanostructures has a relatively high response and a relatively low operating temperature, so it can be expected to serve as a promising functional material in NO_2 gas sensors. The dynamic response curve of the sensor to NO_2 gas was shown in Fig. 9.

Gas-sensing properties of the sensor fabricated with flower-like WO_3 to volatile organic compounds (VOCs) were also investigated. Fig. 10 presents the relationship between the responses to 100 ppm acetone/ethanol/methanol and the operating temperature of the sensor. It is obvious that the operating temperature played an important role on determining the response of sensor to VOCs. At the beginning, the responses of the sensor increased as the operating temperature increased and reached maximum at 300 °C. After that, the responses decreased rapidly with further increasing of the operating temperature. Therefore, 300 °C was considered as the optimum operating temperature and chosen for further examining the gas-sensing properties of the sensor to acetone, ethanol and methanol.

The response and recovery characteristics to 100 ppm acetone/ethanol/methanol at operating temperature of 300 °C were investigated, and the response transients are shown in Fig. 11. The

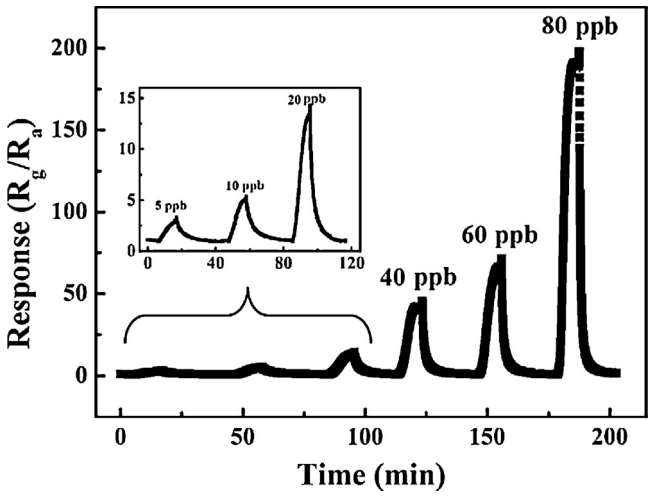

Fig. 9. Dynamic response and recovery curve of the sensor to different concentrations of NO_2 gas at optimum temperature of 90 °C.

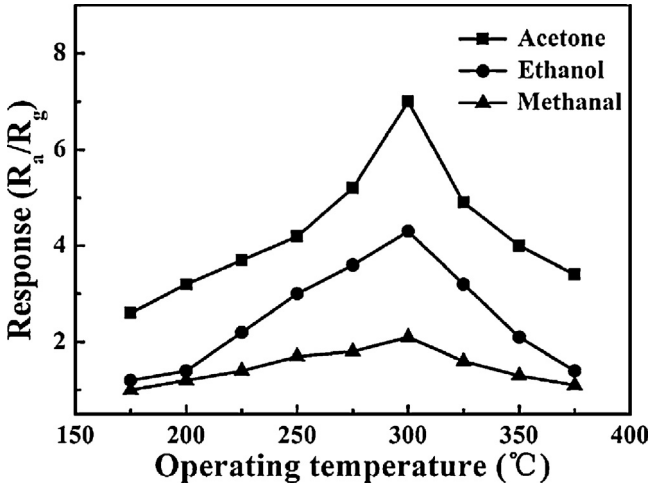

Fig. 10. Response of the sensor to 100 ppm acetone, ethanol and methanol as a function of operating temperature.

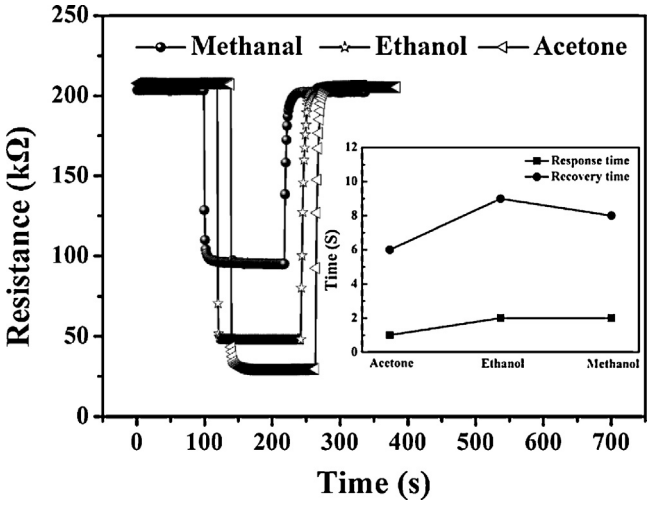

Fig. 11. Response transients of the sensor to 100 ppm acetone, ethanol and methanol at 300 °C, the inset displaying the corresponding response and recovery time.

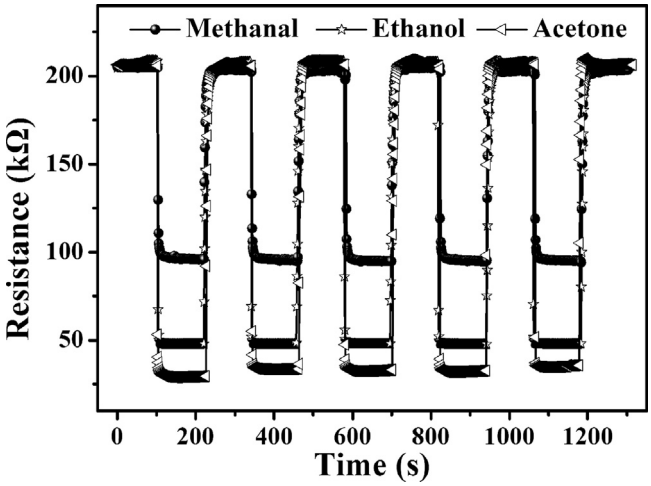

Fig. 12. Five cycles of response curves for 100 ppm acetone, ethanol and methanol at 300 °C.

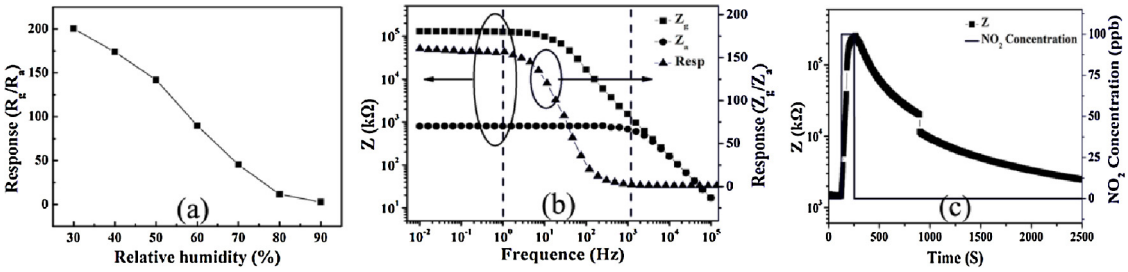

Fig. 13. (a) Responses to 80 ppb NO_2 at different relative humidity, (b) AC responses (Z_g/Z_a) at different testing frequencies and (c) a response and recovery curve to 100 ppb NO_2 measured at 10 Hz.

results indicate that the sensor had a fast response–recovery process. The response and recovery times were about 1/2/2 and 6/9/8 s, respectively, as is shown in the inset of Fig. 11. Compared with the sensing properties of other WO_3 architectures based sensors [35,36], it could be seen that the sensor using flower-like WO_3 structure had a relative shorter response and recovery times. From the application point of view, such as rapid and continuous detection, the sensors should have a fast response and recovery process. So, although our sensor's response was not as high as those reported in some literatures, its advantage of shorter response and recovery times could not be ignored. Five reversible cycles of the response curve indicated that the sensor had good repeatability and stability, as shown in the inset of Fig. 12. The fast response–recovery properties and good repeatability engaged the WO_3-based gas sensor potential applications at the industrial level. There are several factors influence the response and recovery times of the sensor, such as the gas diffusion, the thickness of sensing layer, and the amount of gas adsorption on the sensing material at different operating temperatures [37–39]. At a certain temperature, the amount of target gas and the surface reaction between the gas and the adsorbed oxygen will not vary significantly. Accordingly, the diffusion of oxygen and reducing gases toward the surface of the sensing material could be regarded as the key factor. So we ascribed the fast response and recovery properties to the sensing layer's unconsolidation characteristics.

The gas sensing mechanism of the sensor fabricated of the as-prepared flower-like WO_3 particles should follow the surface charge model, which may be explained by the change in resistance of the sensor upon exposure to different gas atmospheres. If we transfer the sensor from air to an oxidation gas atmosphere like NO_2, NO_2 molecules will take away electrons from the conductance band of WO_3 and cause the sensor's electric resistance increasing. Similarly, when the sensor exposed to a reducing gas such as acetone, these gas molecules can react on the surface of WO_3 nanoparticles and release electrons back to the conduction band, causing the decrease of electric resistance. The possible reasons for the good sensing properties might be attributed to this: the as-prepared WO_3 nanoparticles were relatively dispersive, which leads to a porous sensing layer and provides a good situation for NO_2 molecules to pass through it from top to down easily, in another word, the utility factor of the sensing body should be enhanced. In addition, the high response could be attributed to the good crystallinity of the as-prepared WO_3, as evidenced by the XRD pattern and the SAED image. The good crystallinity guaranteed a good circumstance for electronic transmission, with less electron traps, such as crystal defects, the electron could transfer easier in the material. The result of which was the R_a of the sensor should be small and when the sensor exposed to NO_2 gas, the sensor could provide electrons continuously and its resistance got larger easily.

It is known that humidity may have effects on the response properties at temperature less than 100 °C. To estimate the effects of humidity, we measured the sensor's responses to 80 ppb NO_2 under different relative humidity. From Fig. 13(a) we can see that, increasing the relative humidity, the response decreased. When the relative humidity increased from 30% to 90%, the response decreased from about 200 to 3. This result indicated that the relative humidity really had great effects on the response of the sensor to NO_2. In this paper, we evaluated the DC properties of the sensing material at 90 °C and 30–40% RH, and the gas response was defined as the ratio of the DC electrical resistance in the target gas (R_g) to that in air (R_a). To compare, under the same condition to DC testing, we measured the impedance of the sensor in air and target gas at different frequency to evaluate the response properties of the sensing material to NO_2, the response was defined as the ratio of the impedance in 100 ppb NO_2 (Z_g) to that in air (Z_a). From Fig. 13(b) we can see that when the frequency was between 0.01 Hz and 1 Hz, the gas response was stable. When the test frequency was within 1–1000 Hz, the response of the sensor decreased with the increase of frequency. However, when the test frequency was higher than 1000 Hz, the sensor showed no response to NO_2. Fig. 13(c) shows a response and recovery curve measured at 10 Hz, 90 °C and 30–40% RH. As can be seen, the response time was relatively short, however, the recovery time was ultra long. So it is a drawback of AC test, which cannot be ignored. The reason to this phenomenon is not clear, needing further study.

4. Conclusion

Dispersive flower-like WO_3 architectures composed of nanorods were synthesized successfully by calcining $W_{18}O_{49}$ nanowires prepared by a microwave-assisted solvothermal method. The sensor fabricated from the as-prepared WO_3 showed high response and good selectivity to ppb level NO_2 at 90 °C. Besides, the sensor exhibited fast response and recovery process to 100 ppm acetone at 300 °C. The gas-sensing mechanism was also briefly introduced. These results suggest that our sensor has potential applications in low concentration NO_2 detection and fast acetone detection.

Acknowledgments

This work was supported by Natural Science Foundation of China (Nos. 21001051, 61074172, 61134010), Program for Chang jiang Scholars and Innovative Research Team in University (No. IRT1017), and Jilin Province Science and Technology Development Plan Program (20106002).

References

[1] M.O. Coppens, J. Sun, T. Maschmeyer, Synthesis of hierarchical porous silicas with a controlled pore size distribution at various length scales, Catal. Today 69 (2001) 331–335.
[2] W. Cai, J. Yu, M. Jaroniec, Template-free synthesis of hierarchical spindle-like γ-Al_2O_3 materials and their adsorption affinity towards organic and inorganic pollutants in water, J. Mater. Chem. 20 (2010) 4587–4594.

[3] F. Xu, Y. Wang, X. Wang, Y. Zhang, Y. Tang, P. Yang, A novel hierarchical nanozeolite composite as sorbent for protein separation in immobilized metal-ion affinity chromatography, Adv. Mater. 15 (2003) 1751–1753.
[4] B. Bhushan, K. Koch, Y.C. Jung, Biomimetic hierarchical structure for self-cleaning, Appl. Phys. Lett. 93 (2008) 093101–093103.
[5] M. Mo, J.C. Yu, L. Zhang, S.K.A Li, Self-assembly of ZnO nanorods and nanosheets into hollow microhemispheres and microspheres, Adv. Mater. 17 (2005) 756–760.
[6] S.W. Kim, M. Kim, W.Y. Lee, T. Hyeon, Fabrication of hollow palladium spheres and their successful application to the recyclable heterogeneous catalyst for Suzuki coupling reactions, J. Am. Chem. Soc. 124 (2002) 7642–7643.
[7] Y. Xiong, B. Wiley, J. Chen, Z.Y. Li, Y. Yin, Y. Xia, Corrosion-based synthesis of single-crystal Pd nanoboxes and nanocages and their surface plasmon properties, Angew. Chem. Int. Ed. 44 (2005) 7913–7917.
[8] G.Z. Shen, Y. Bando, C.J. Lee, Synthesis and evolution of novel hollow ZnO urchins by a simple thermal evaporation process, J. Phys. Chem. B 109 (2005) 10578–10583.
[9] A.S. Shaporev, V.K. Ivanov, A.E. Baranchikov, Y.D. Tret'yakov, Microwave-assisted hydrothermal synthesis and photocatalytic activity of ZnO, Inorg. Mater. 43 (2007) 35–39.
[10] X. Hu, J. Gong, L. Zhang, J.C. Yu, Continuous size tuning of monodisperse ZnO colloidal nanocrystal clusters by a microwave-polyol process and their application for humidity sensing, Adv. Mater. 20 (2008) 4845–4850.
[11] X. Hu, J.C. Yu, J. Gong, Q. Li, G. Li, α-Fe_2O_3 nanorings prepared by a microwave-assisted hydrothermal process and their sensing properties, Adv. Mater. 19 (2007) 2324–2349.
[12] S.W. Cao, Y.J. Zhu, M.Y. Ma, L. Li, L. Zhang, Hierarchically nanostructured magnetic hollow spheres of Fe_3O_4 and γ-Fe_2O_3: preparation and potential application in drug delivery, J. Phys. Chem. C 112 (2008) 1851–1856.
[13] D.P. Volanti, D. Keyson, L.S. Cavalcante, A.Z. Simões, M.R. Joya, E. Longo, Synthesis and characterization of CuO flower-nanostructure processing by a domestic hydrothermal microwave, J. Alloys Compd. 459 (2008) 537–542.
[14] D.P. Volanti, M.O. Orlandi, J. Andres, E. Longo, Efficient microwave-assisted hydrothermal synthesis of CuO sea urchin-like architectures via a mesoscale self-assembly, Cryst. Eng. Commun. 12 (2010) 1696–1699.
[15] X. Feng, J.D. Sloppy, T.J. LaTempa, M. Paulose, S. Komarneni, N. Bao, Synthesis and deposition of ultrafine Pt nanoparticles within high aspect ratio TiO_2 nanotube arrays: application to the photocatalytic reduction of carbon dioxide, J. Mater. Chem. 21 (2011) 13429–13433.
[16] H.E. Wang, L.X. Zheng, C.P. Liu, Y.K. Liu, C.Y. Luan, H. Cheng, Rapid microwave synthesis of porous TiO_2 spheres and their applications in dye-sensitized solar cells, J. Phys. Chem. C 115 (2011) 10419–10425.
[17] H.W. Wang, C.H. Kuo, H.C. Lin, I.T. Kuo, C.F. Cheng, Rapid formation of active mesoporous TiO_2 photocatalysts via micelle in a microwave hydrothermal process, J. Am. Ceram. Soc. 89 (2006) 3388–3392.
[18] T. Yanagimoto, Y.T. Yu, K. Kaneko, Microstructure and CO gas sensing property of Au/SnO_2 core–shell structure nanoparticles synthesized by precipitation method and microwave-assisted hydrothermal synthesis method, Sens. Actuators B 166–167 (2012) 31–35.
[19] T. Kida, A. Nishiyama, M. Yuasa, K. Shimanoe, N. Yamazoe, Highly sensitive NO_2 sensors using lamellar-structured WO_3 particles prepared by an acidification method, Sens. Actuators B 135 (2009) 568–574.
[20] Q. Xiang, G.F. Meng, H.B. Zhao, Y. Zhang, H. Li, W.J. Ma, Au nanoparticle modified WO_3 nanorods with their enhanced properties for photocatalysis and gas sensing, J. Phys. Chem. C 114 (2010) 2049–2055.
[21] C.C. Chan, W.C. Hsu, C.C. Chang, C.S. Hsu, Hydrogen incorporation in gasochromic coloration of sol–gel WO_3 thin films, Sens. Actuators B 157 (2011) 504–509.
[22] F. Liu, L. Li, F. Mo, J. Chen, S. Deng, N. Xu, A catalyzed-growth route to directly form micropatterned WO_2 and WO_3 nanowire arrays with excellent field emission behaviors at low temperature, Cryst. Growth Des. 10 (2010) 5193–5199.
[23] H. Zheng, Y. Tachibana, K. Kalantar-zadeh, Dye-sensitized solar cells based on WO_3, Langmuir 26 (2010) 19148–19152.
[24] X.L. Li, T.J. Lou, X.M. Sun, Y.D. Li, Highly sensitive WO_3 hollow-sphere gas sensors, Inorg. Chem. 43 (2004) 5442–5449.
[25] J.C. Yang, P.K. Dutta, Solution-based synthesis of efficient WO_3 sensing electrodes for high temperature potentiometric NO_x sensors, Sens. Actuators B 136 (2009) 523–529.
[26] C.S. Blackman, I.P. Parkin, Atmospheric pressure chemical vapor deposition of crystalline monoclinic WO_3 and WO_{3-x} thin films from reaction of WCl_6 with O-containing solvents and their photochromic and electrochromic properties, Chem. Mater. 17 (2005) 1583–1590.
[27] J. Wang, E. Khoo, P.S. Lee, J. Ma, Controlled synthesis of WO_3 nanorods and their electrochromic properties in H_2SO_4 electrolyte, J. Phys. Chem. C 113 (2009) 9655–9658.
[28] A. Yan, C. Xie, D. Zeng, S. Cai, M. Hu, Synthesis, formation mechanism and sensing properties of WO_3 hydrate nanowire netted-spheres, Mate. Res. Bull. 45 (2010) 1541–1547.
[29] A. Yella, U.K. Gautam, E. Mugnaioli, M. Panthofer, Y. Bando, D. Golberg, Asymmetric tungsten oxide nanobrushes via oriented attachment and Ostwald ripening, Cryst. Eng. Commun. 13 (2011) 4074–4081.
[30] N. Yamazoe, G. Sakai, K. Shimanoe, Oxide semiconductor gas sensors, Catal. Surv. Asia 7 (2003) 63–75.
[31] L. You, Y.F. Sun, J. Ma, Y. Guan, J.M. Sun, Y. Du, G.Y. Lu, Highly sensitive NO_2 sensor based on square-like tungsten oxide prepared with hydrothermal treatment, Sens. Actuators B 157 (2011) 401–407.
[32] Y.G. Choi, G. Sakai, K. Shimanoe, N. Yamazoe, Wet process-based fabrication of WO_3 thin film for NO_2 detection, Sens. Actuators B 101 (2004) 107–111.
[33] M. Yuasa, Y. Matoba, N. Yamazoe, K. Shimanoe, Wet process-preparation of Re-doped WO_3 for wide range of NO_2 detection, J. Ceram. Soc. Jpn. 118 (2010) 184–187.
[34] C. Zhang, A. Boudiba, C. Navio, M.G. Olivier, R. Snyders, M. Debliquy, Study of selectivity of NO_2 sensors composed of WO_3 and MnO_2 thin films grown by radio frequency sputtering, Sens. Actuators B 161 (2012) 914–922.
[35] G.F. Meng, Q. Xiang, Q.Y. Pan, J.Q. Xu, The selective acetone detection based on Fe_3O_4 doped WO_3 nanorods, Sens. Lett. 9 (2011) 128–131.
[36] D. Chen, X. Hou, T. Li, L. Yin, B. Fan, H. Wang, Effects of morphologies on acetone-sensing properties of tungsten trioxide nanocrystals, Sens. Actuators B 153 (2011) 373–381.
[37] G. Korotcenkov, B.K. Cho, Thin film SnO_2-based gas sensors: film thickness influence, Sens. Actuators B 142 (2009) 321–330.
[38] G. Korotcenkov, V. Brinzari, J.R. Stetter, I. Blinov, V. Blaja, The nature of processes controlling the kinetics of indium oxide-based thin film gas sensor response, Sens. Actuators B 128 (2008) 51–63.
[39] G. Korotcenkov, M. Ivanov, I. Blinov, J.R. Stetter, Kinetics of indium oxide-based thin film gas sensor response: the role of redox and adsorption/desorption processes in gas sensing effects, Thin Solid Films 515 (2007) 3987–3996.

Biographies

Zhenyu Wang received his BS degree from the Electronics Science and Engineering Department, Jilin University, China in 2010. Presently, he is a PhD student, majored in microelectronics and solid state electronics. Now, he is engaged in the synthesis and characterization of the semiconducting functional materials and gas sensors.

Peng Sun received his MS degree from State Key Laboratory of Superhard Materials, Jilin University, China in 2009. He entered the PhD course in 2010, majored in microelectronics and solid state electronics. Now, he is engaged in the synthesis and characterization of the semiconducting functional materials and gas sensors.

Tianlin Yang received his BS degree from the Electronics Science and Engineering department, Jilin University, China in 2012. Presently, he is a graduate student, majored in microelectronics and solid state electronics.

Yuan Gao received her Doctor's degree in Department of Analytical Chemistry at Jilin University in 2012. Now she is a lecturer in Jilin University, China. Her current research is focus on the preparation and application of graphene oxide and semiconductor oxide, especial in gas sensor and biosensor.

Xiaowei Li received his BS degree from the Electronics Science and Engineering Department, Jilin University, China in 2011. Presently, he is a graduate student, majored in Integrated Circuit Engineering.

Geyu Lu received his BS and MS degree in electronic sciences from Jilin University, China in 1985 and 1988, respectively, and PhD degree in 1998 from Kyushu University in Japan. Now he is a professor of Jilin University, China. Presently, he is interested in the development of functional materials and chemical sensors.

Yu Du received her PhD from chemistry of Jilin University, China in 2006. After that, she had been working as the Postdoctoral at Nanyang Technological University, Singapore for about two years. She is currently an Associate Professor at the Department of Applied Physics in Shenzhen University, China.